












RESEARCH ARTICLE | MAY 30 2024

**Composition-dependent spin exchange interaction for
multiferroicity in perovskite $\text{Pb}(\text{Fe}_{1/2}\text{Nb}_{1/2})\text{O}_3$**

Ji-Hun Park ; Jae-Hyeon Cho ; Frederick P. Marlon; Haeseong Jang ; Ju-Hyeon Lee ;
Jongmoon Jang ; Geon-Tae Hwang ; Abhijit Pramanick ; Mads Ry Vogel Jørgensen ; Min Gyu Kim ;
Wook Jo  

*J. Appl. Phys.* 135, 204102 (2024)<https://doi.org/10.1063/5.0211130>**Articles You May Be Interested In**

Room temperature magnetoelectric coupling in $\text{Pb}(\text{Fe}_{1/2}\text{Nb}_{1/2})\text{O}_3$ by counterbalancing imbalanced spin moments through spin canting

J. Appl. Phys. (September 2021)

Composition-dependent spin exchange interaction for multiferroicity in perovskite $\text{Pb}(\text{Fe}_{1/2}\text{Nb}_{1/2})\text{O}_3$

Cite as: J. Appl. Phys. 135, 204102 (2024); doi: 10.1063/5.0211130

Submitted: 29 March 2024 · Accepted: 16 May 2024 ·

Published Online: 30 May 2024



Ji-Hun Park,¹ Jae-Hyeon Cho,¹ Frederick P. Marlton,² Haeseong Jang,³ Ju-Hyeon Lee,¹ Jongmoon Jang,⁴ Geon-Tae Hwang,⁵ Abhijit Pramanick,⁶ Mads Ry Vogel Jørgensen,⁷ Min Gyu Kim,³ and Wook Jo^{1,a)}

AFFILIATIONS

¹Department of Materials Science and Engineering, Ulsan National Institute of Science and Technology (UNIST), Ulsan 44919, Republic of Korea

²Centre for Clean Energy Technology, School of Mathematical and Physical Sciences, Faculty of Science, University of Technology Sydney, Sydney, NSW 2007, Australia

³Beamline Research Division, Pohang Accelerator Laboratory (PAL), Pohang 37673, Republic of Korea

⁴Department of Functional Ceramics, Korea Institute of Materials Science (KIMS), Changwon 51508, Republic of Korea

⁵Department of Materials Science and Engineering, Pukyong National University, Busan 42601, Republic of Korea

⁶Group of Electrical and Electronic Engineers, Paris, University Paris-Saclay, Gif-sur-Yvette, France

⁷Department of Chemistry and iNANO, Aarhus University, Aarhus C 8000, Denmark and MAX IV Laboratory, Lund University, SE-221 00 Lund, Sweden

^{a)}Author to whom correspondence should be addressed: wookjo@unist.ac.kr

ABSTRACT

The composition-dependent spin exchange interaction in a perovskite-structured $\text{Pb}(\text{Fe}_{0.5-x}\text{Ni}_x)\text{Nb}_{1/2}\text{O}_3$ system has been studied to understand its multiferroicity at room-temperature. Special emphasis was paid to the magnetic behavior in terms of magnetic moment, interatomic distance, and atomic ordering because they play a key role in the modulation of magnetic multiferroic behavior. We observed that 10 mol.% Ni incorporation led to multiferroic behavior with considerable ferrimagnetic properties (saturation magnetization of 0.6 emu/g and a coercive field of 20 Oe) coupled with the inherent properties of displacive ferroelectricity (spontaneous polarization of $20 \mu\text{C}/\text{cm}^2$). A subsequent increase in the Ni substitution degree degraded the ferroelectricity due to a phase transition from a non-centrosymmetric rhombohedral to a centrosymmetric cubic system. We have shown that magnetic spins with a pronounced magnetic moment along the [001] direction are ferrimagnetically arranged when the interatomic distance between the magnetic transition metals at the octahedral site is less than 4 Å, resulting in significant magnetic properties. The objective of this study is to provide a general methodology for modulating magnetic orders in ferroelectric perovskite oxides.

© 2024 Author(s). All article content, except where otherwise noted, is licensed under a Creative Commons Attribution-NonCommercial 4.0 International (CC BY-NC) license (<https://creativecommons.org/licenses/by-nc/4.0/>). <https://doi.org/10.1063/5.0211130>

I. INTRODUCTION

Magnetoelectric (ME) multiferroics, which exhibit ferromagnetism coupled with simultaneous ferroelectricity in a single phase, have garnered significant research interest in both physical investigation and novel applications, such as multi-state memory and

photovoltaics.^{1–8} It is widely accepted that multiferroics are classified as either type I or type II depending on the origin of their ferroic orders.^{9–11} Type I multiferroics have distinct ferroic origins, whereas the multiferroicity of type II materials is solely caused by magnetic spin interactions. Type I multiferroic oxides have received

23 January 2025 05:53:53

considerable attention for practical applications owing to their remarkable ferroelectric properties and high ferroic transition temperatures, particularly in perovskite-structured oxides, such as bismuth ferrite.^{12–17} Unfortunately, due to their atomic configuration, perovskite multiferroics generally exhibit an antiferromagnetic or weakly ferromagnetic order at and above room temperature.^{18,19} The perovskite structure (ABO_3), which has 12- and 6-coordinated sites for cations, only enforces a linear superexchange interaction between magnetic spins because magnetic ions, i.e., transition metals, are preferentially placed at the six-coordinate site owing to their relatively small ionic sizes, according to the Goldschmidt tolerance factor.^{20–22} This means that the inherent magnetic nature of perovskite multiferroics is constrained to be antiferromagnetic according to the Goodenough–Kanamori rules, which limits their use in practical applications because the magnetic field required to induce a useful magnetic moment is too large when magnetic spins are antiferromagnetically arrangement.^{23–25} To overcome this limitation, numerous experiments have been performed focusing on the induction of ferromagnetism with a significant net magnetic moment in this structure.^{1–3,17,26} However, most previous attempts have only provided an experimental dataset without a sufficient explanation as to why such magnetic properties were induced. Therefore, this study focuses on a composition-dependent spin exchange interaction. It provides a clue to understanding the origin of the induced magnetic properties in perovskite-structured multiferroic oxides, and we expect that it would usher in the voltage-driven spin-controlled memory applications.

Lead iron niobate $\text{PbFe}_{1/2}\text{Nb}_{1/2}\text{O}_3$ (PFN) is a perovskite-structured type I multiferroic oxide with an embedded antiferromagnetic order (Néel temperature $T_N = 150$ K) and a displacive ferroelectric order (ferroelectric Curie temperature $T_{C,FE} = 380$ K).²⁷ Recently, notable magnetic properties while maintaining the displacive ferroelectricity at room temperature were induced in PFN by partially replacing the Fe ions present with distinct magnetic ions, such as Ni and Mn ions.¹⁰ The magnetic properties peaked when 10 mol. % Ni was replaced by Fe. However, the reason why PFN with 10 mol. % Ni substitution exhibited a larger magnetic moment than 20 mol. % was not clearly explained, although the magnetic moment at 25 mol. % Ni substitution should be maximized from the perspective of the proposed mechanism, i.e., by ferromagnetic order induced by an unbalanced spin configuration consisting of distinct spins with different Bohr magneton values. Here, we have prepared whole series of Fe-site-engineered PFN compositions with different Fe/Ni ratios by replacing Ni for Fe, i.e., $\text{Pb}(\text{Fe}_{0.5-x}\text{Ni}_x)\text{Nb}_{1/2}\text{O}_3$ (PFNN100x, $x = 0, 0.1, 0.2, 0.3, 0.4, 0.5$), and investigated the spin moment, atomic ordering, and interatomic distance of magnetic ions present, all of which are closely related to the spin exchange interaction, to elucidate their multiferroicity. In addition to this series, an experimental dataset for the PFNN5, 15, and 25 compositions is provided in the [supplementary material](#) to demonstrate the consistency of the results. We first revealed multiferroic properties and demonstrated their origins by employing x-ray diffraction, x-ray absorption spectroscopy, and neutron powder diffraction.

II. EXPERIMENTAL PROCEDURE

The bulk ceramic PFNN100x series was prepared by a solid-state reaction method using dried raw powders, i.e., PbO (99.9%,

Alfa-Aesar), NiO (99%, Alfa-Aesar), Fe_2O_3 (99%, Sigma-Aldrich), and Nb_2O_5 (99.99%, Sigma-Aldrich). The precursor powders were mixed according to their stoichiometric chemical composition and ball-milled in ethanol (99.99%) with YSZ balls for 24 h. After drying in an oven at 373 K, the ball-milled mixtures were calcined at 923 K for 2 h. After addition of polyvinyl alcohol (PVA) as a binder, the calcined powders were sieved with a mesh size of $150\ \mu\text{m}$ and compacted into pellets. The pellets were sintered at 1223–1323 K for 2 h and then shaped into different forms into various shapes for characterization: square pieces for magnetic properties, disk-shaped pellets coated with silver electrodes for ferroelectric properties, and crushed and thermally annealed powders for structural analysis.

A vibrating specimen magnetometer (VSM7300) was used to obtain magnetic hysteresis loops at room temperature. Ferroelectric properties were measured using a ferroelectric measurement system (aixACCT, aixPES) at an applied electric field of 3 kV/mm and a measurement frequency of 50 Hz. A magnetoelectric (ME) measurement system, consisting of lock-in (SR850), bipolar (BA4825), and current (BOP 36-12ML) amplifiers together with an electromagnet for the DC field and a Helmholtz coil for the AC field, were used to obtain the ME coefficients of electrically poled samples at room temperature. X-ray diffraction (XRD, D/MAX2500 V/PC) with $\text{Cu-K}\alpha$ radiation was used to obtain structural information. X-ray absorption near edge structure (XANES) and extended x-ray absorption fine structure (EXAFS) data were measured at the BL10C beam line (WEXAFS) in the Pohang Light Source (PLS-II) using the top-up mode operation, with a ring current of 250 mA at 3.0 GeV. Phase correction was performed by adding $0.4\ \text{\AA}$ to the obtained interatomic distance when transforming the EXAFS profiles.^{28,29} The incident x-ray intensity was reduced to approximately 30% to avoid contamination by higher-order harmonics. Energy calibration was conducted for each measurement using reference transition-metal foils. The obtained x-ray absorption spectroscopy (XAS) data were normalized using AUTOBK and FEFFIT software in the UWXAFS package. Neutron total scattering data were measured using a nanoscale ordered materials diffractometer (NOMAD) at the Spallation Neutron Source (SNS) located at Oak Ridge National Laboratory (ORNL). Samples were crushed to powder and placed in 6 mm vanadium cans. The data were corrected for instrument background, incident neutron spectrum, absorption, and multiple scattering and finally normalized. A Q_{max} value of $34\ \text{\AA}^{-1}$ was used to calculate the pair distribution function (PDF). Bragg Rietveld refinements of the four highest-resolution detector banks and PDF small-box modeling were performed using TOPAS.³⁰ The total scattering data were transformed to the pair distribution function (PDF), $G(r)$, using a sine Fourier transform. This transformation was performed using software internal to ORNL.

III. RESULTS AND DISCUSSION

The magnetic hysteresis (MH) loops of PFNN100x series were prepared to study the variation of magnetic properties as a function of Fe to Ni ion ratio (see Fig. 1). The magnetic behavior of PFNN0, i.e., pristine PFN, indicates an antiferromagnetic order at room temperature, although its Néel temperature is known to be 150 K.

23 January 2025 05:53:53

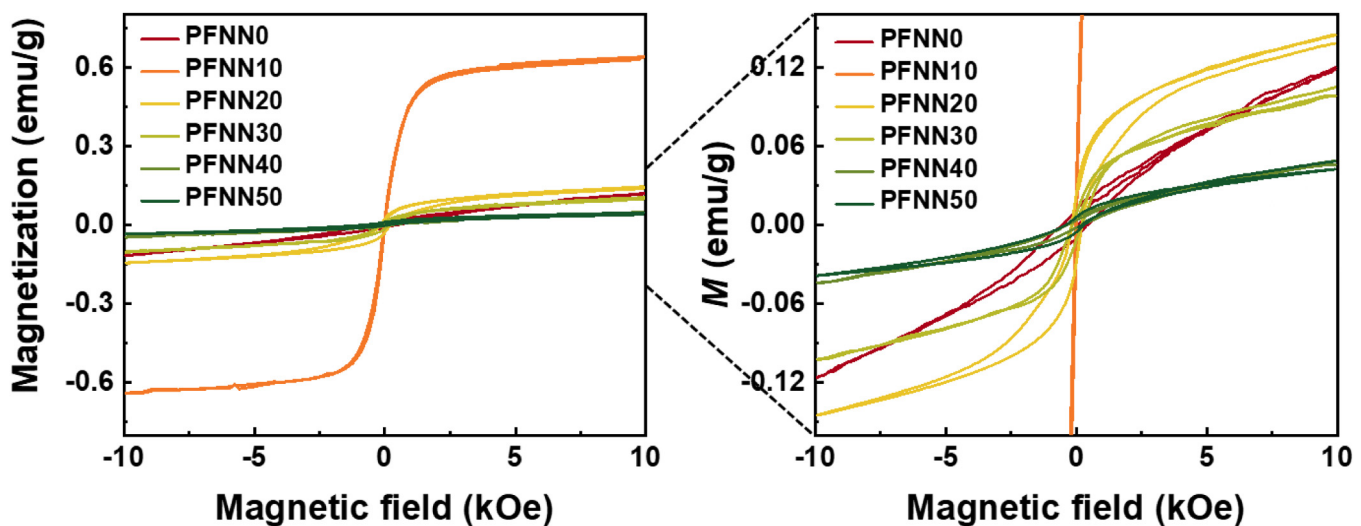


FIG. 1. Magnetic hysteresis (MH) loops of PFNN100x series at room temperature. The magnified view of the MH loops was created to show the detailed magnetic behavior of all compositions.

This discrepancy could be due to the complex and subtle nature of bulk polycrystalline and/or magnetic spin-glass effects that make PFN a relaxor multiferroic.^{14,27,31–33} The saturated MH loop, which is the inherent nature of ferromagnetic order, was observed from PFNN10 to PFNN30, whereas the others exhibited antiferromagnetic behavior. The saturation magnetization value peaked at PFNN10 (0.6 emu/g), followed by a dramatic decrease with an increasing Ni substitution level. It is noted that the superiority of PFNN10 in terms of the coercive field is more pronounced; the coercive field values of PFNN0, PFNN10, PFNN20, PFNN30, PFNN40, and PFNN50 were 470, 20, 190, 190, 222, and 450 Oe, respectively [the magnetic properties of PFNN5 and PFNN15 are shown in Fig. S1(a) of the [supplementary material](#)]. The obtained MH loops indicate that only PFNN10 exhibits a soft ferromagnetic order, namely, a ferrimagnetic order as well as a displacive ferroelectricity with an ME coupling (Figs. 2 and S2 in the [supplementary material](#)), while PFNN20 and PFNN30 appear weak ferromagnetic, and the others are antiferromagnetic.

The observed change in the magnetization and coercive field values as a function of the level of Ni incorporation is not sufficient to explain the previously proposed spin-canting-induced unbalanced spin moment.^{34–41} In this case, the saturation magnetization value should have peaked at PFNN25; PFNN25 exhibits weak ferromagnetic behavior with a magnetization value somewhere between PFNN20 and PFNN30 [Fig. S1(b) in the [supplementary material](#)]. Since the Fe-to-Ni ratios of PFNN40 and PFNN10 are 1:4 and 4:1, respectively, PFNN40 should exhibit a substantial magnetization value with a low coercive field. Notably, PFNN40 exhibits an antiferromagnetic nature with a high coercive field value. This unexpected behavior suggests that not only the remanent spin moment from the spin cancellation between Fe and Ni ions, but also additional factors, such as interatomic distance and atomic ordering, related to the spin arrangement, play a key role in inducing the

significant magnetic properties measured in PFNN10. This suggestion is supported by the fact that the value of the coercive field value in PFNN10 decreased approximately 24-fold and then returned to a value similar to that of the pristine sample.

A well-saturated polarization hysteresis loop was obtained for PFNN0, PFNN10, and PFNN20 at room temperature, demonstrating the presence of a ferroelectric order, whereas the others became to exhibit paraelectric behavior (see Fig. 2); PFNN30, PFNN40, and PFNN50 are not relaxor ferroelectrics by considering the temperature-dependent dielectric constant, as demonstrated in the previous study.¹⁰ Both the maximum and remanent polarizations tend to decrease with increasing substitution level, whereas the coercive field peaks at PFNN10. Considering that Ni substitution could lead to structural transformation according to the Goldschmidt tolerance factor, the degradation in ferroelectricity appears to be caused by phase transformation from rhombohedral to cubic perovskite structures. This conjecture is supported by the decrease in the Curie temperature with increasing substitution levels, as reported in a previous study.¹⁰ The presence of ferroelectric order in PFNN0, PFNN10, and PFNN20 is also confirmed by the corresponding electromechanical strain hysteresis loops, which exhibit a butterfly shape typical of normal ferroelectrics. The S_{\max}/E_{\max} value, which is the figure of merit for high-stroke piezoelectric applications, is approximately 240 pm/V at 3 kV/mm, which is greater than that of the pristine material (180 pm/V).

Figure 3 shows the x-ray diffraction (XRD) patterns measured to determine the atomic structure of all PFNN100x compositions. It is noted that all PFNN100x exhibit a single-phase perovskite structure as the main phase, while the secondary phases, i.e., pyrochlore and NiO phase, first appeared in PFNN20 and then gradually increased as the Ni substitution level became higher. Since pyrochlore and NiO are known to be paramagnetic and antiferromagnetic oxides, respectively, we excluded the effect of the

23 January 2025 05:53:53

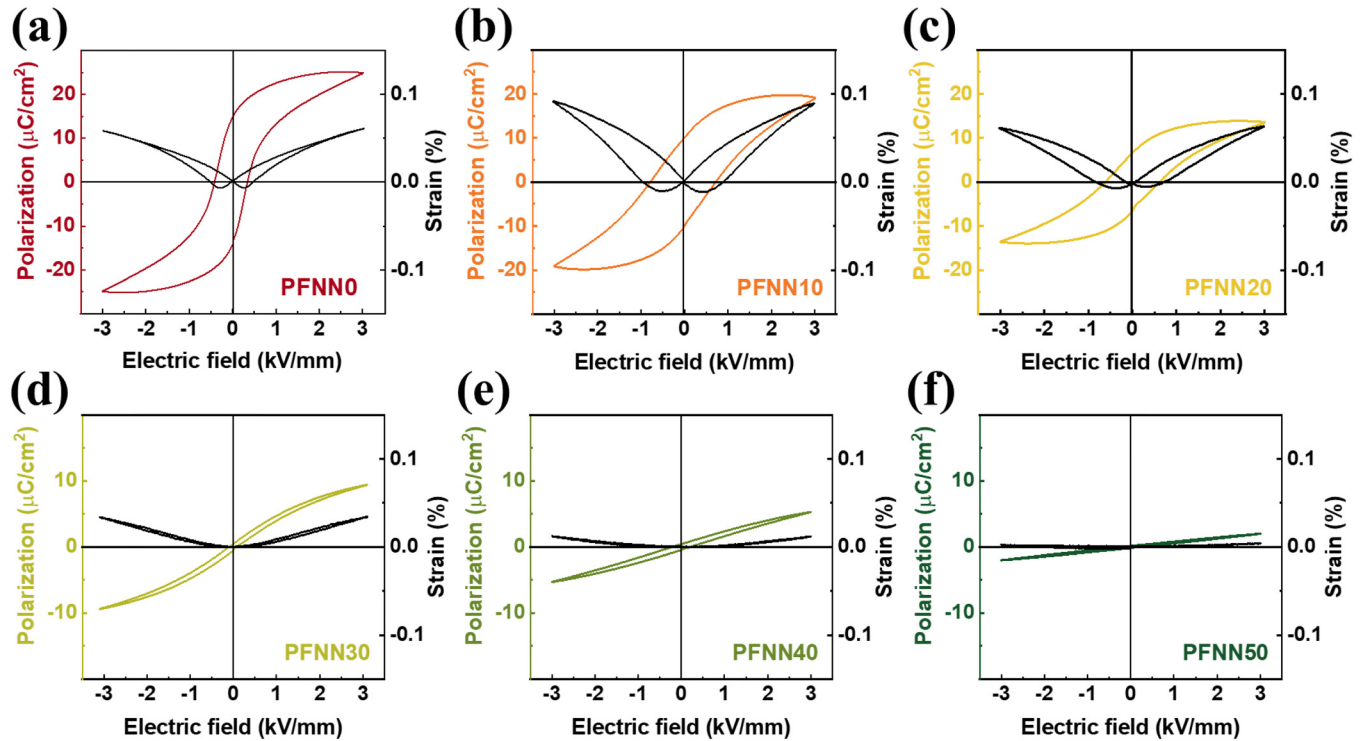


FIG. 2. Ferroelectric and electromechanical strain hysteresis loops of (a) pristine PFN, (b) PFNN10, (c) PFNN20, (d) PFNN30, (e) PFNN40, and (f) PFNN50 at room-temperature measured by applying an electric field of up to 3 kV/mm at a measurement frequency of 50 Hz.

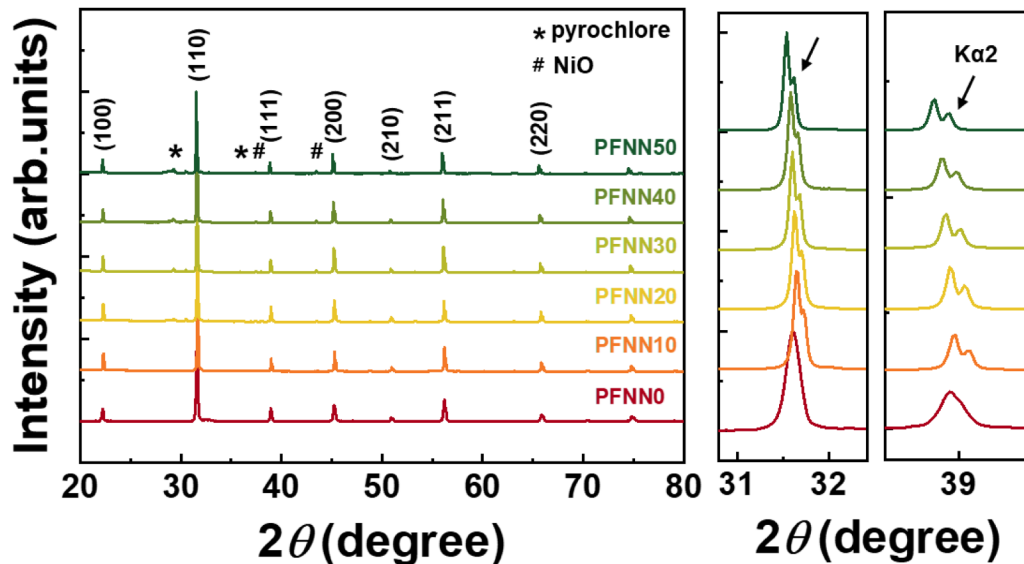


FIG. 3. X-ray diffraction (XRD) patterns of the PFNN100x series showing a magnified view of (110) and (111) peaks. The secondary phase peaks were marked in the profiles with the asterisk and pound symbols representing pyrochlore and NiO, respectively.

secondary phases when discussing the composition-dependent changes in magnetic behavior.^{42–44} The reason is that the order of the magnetic moment of them is much lower than that of the obtained MH loops. It was found that the lattice constant decreased at PFNN10 and gradually increased to become larger at PFNN50 than that of PFNN0 when the peak shift is considered in conjunction with Bragg's law (see also Fig. S3 in the [supplementary material](#)). This indicates that the interatomic distance in PFNN10 is shorter than that of the others, while the average lattice constant is approximately 4 Å. Given the ionic radius of the Fe^{3+} and Ni^{3+} ions (0.645 and 0.600 Å, respectively), the increased lattice parameter after PFNN10 is implausible. This could be interpreted as the transition metals present being partially reduced to 2+ ions, i.e., Fe^{2+} (0.78 Å) and Ni^{2+} (0.69 Å), which is accompanied by the formation of oxygen vacancies that could increase the lattice parameter;^{45–48} note that this reduction occurs only in the case of the Ni ion as shown by the x-ray absorption spectra in Fig. 4. This reduction denotes that the net magnetic moment would be enhanced as Ni substitution doses up to PFNN25, considering the Bohr magneton of each ion and their spin cancellation; $5.92\mu_B$ for

Fe^{3+} , $3.87\mu_B$ for Ni^{3+} , and $2.83\mu_B$ for Ni^{2+} . However, as shown in Fig. 1, the saturation magnetization peaked at PFNN10. These results suggest that magnetic ions with distinct magnetic moments should be ordered and positioned with an interatomic distance of less than 4 Å to form a ferrimagnetically aligned spin configuration in perovskite oxides.

To determine the superexchange interaction between magnetic ions in the PFNN100x series, x-ray absorption spectroscopy (XAS), including x-ray absorption near edge structure (XANES) and extended x-ray absorption fine structure (EXAFS), was utilized to ascertain the ionic charge state and interatomic distance (Figs. 4 and S3 in the [supplementary material](#)). It is well known that the pre-edge peak originates from the local electric transition from 1s to 3d orbitals, induced by orbital hybridization, primarily attributable to structural distortions.⁴⁹ In view of this, XANES at the Fe and Ni K-edge profiles denotes the structural transition to the centrosymmetric system by decreasing the intensity of the pre-edge peak at 7115 eV, while that of the main peak at 7135 eV increases, which is consistent with previous results.^{10,50–52} It was observed that the charge state of Fe ions is nearly the same in all

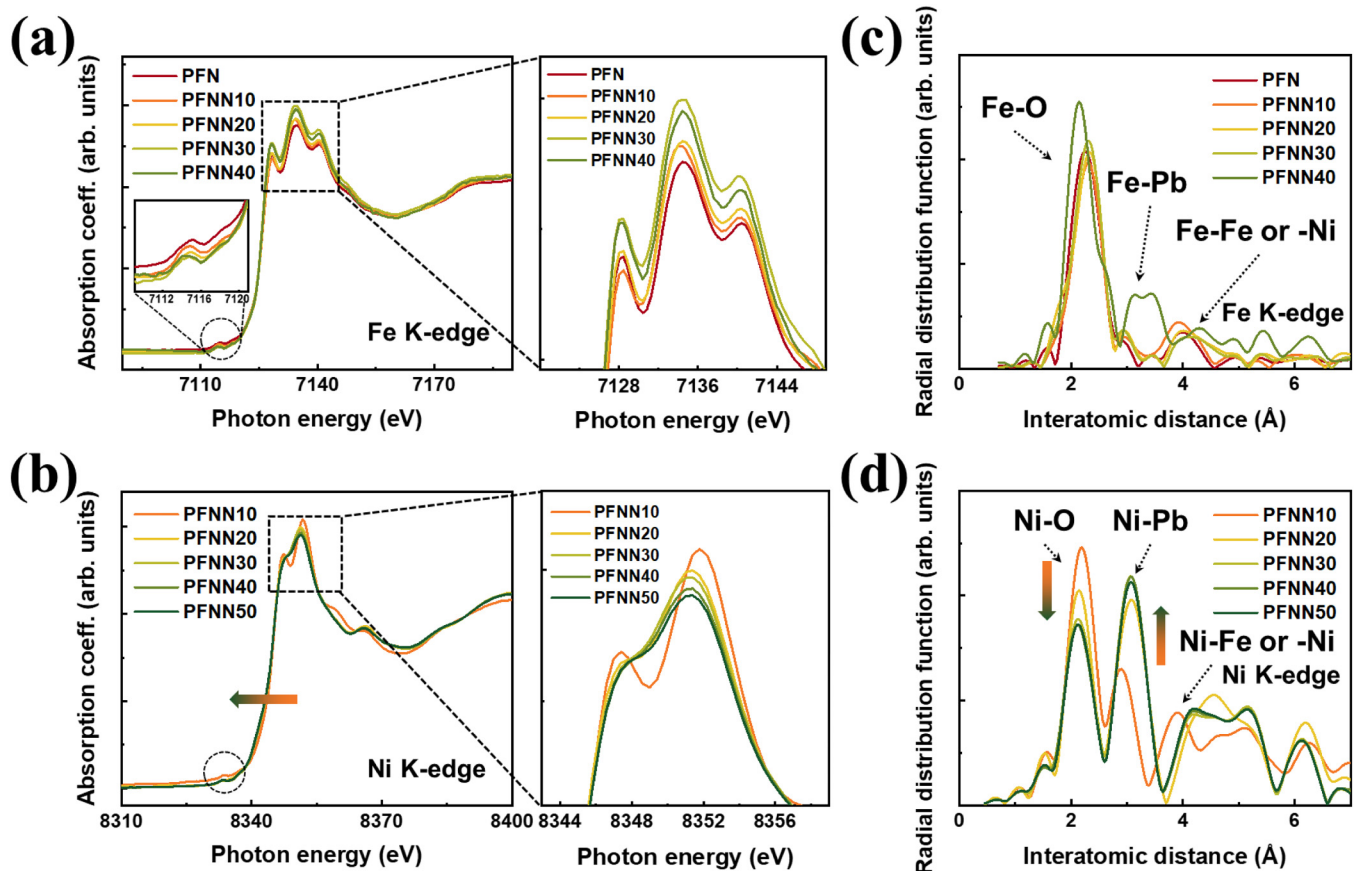


FIG. 4. X-ray absorption spectroscopy (XAS) of PFNN100x series. X-ray absorption near edge structure (XANES) at the (a) Fe/(b) Ni K-edge with a magnified view around the main peak. Extended x-ray absorption fine structure (EXAFS) showing the interatomic distances between the (c) Fe/(d) Ni ion and its neighboring ions.

23 January 2025 05:53:53

compositions, except for PFNN40, as shown by the main peaks of XANES and the Fe–O contribution of EXAFS at the Fe K-edge profiles, whereas this is not the case for Ni ions. The sudden change in the oxidation state of the Fe ion and the distance between Fe and its neighboring ions in PFNN40 might be due to the phase transition from rhombohedral to pseudo-cubic and/or the presence of a significant number of secondary phases. Given the perturbations in the XANES profiles at the Ni K-edge, i.e., the shift to the left in the overall peak and the change in the intensity ratio of the two main peaks (8347 and 8352 eV), the Ni ion was reduced with increasing degree of substitution level,^{53,54} suggesting that the increase in the lattice constant after PFNN10 is due to the reduction of Ni ions. Interestingly, the oxidation state of the Ni ion in PFNN10 is obviously different from that of the others, considering the intensity ratio of the main peaks in the EXAFS at the Ni K-edge profiles and that of the Ni–O and Ni–Pb contributions in the XANES at the Ni K-edge profiles. Furthermore, the interatomic distance between the Ni ions and their neighbors in PFNN10 is apparently different from that of the others. The interatomic distance between Ni–Fe or –Ni of PFNN10 is approximately 3.9 Å, while that of the others is approximately 4.0 Å. Considering that the EXAFS spectra were obtained for a single element (in this case, Fe and Ni ions), this implies that the Ni ions in PFNN10 may be displaced to be close to

each other in short-range order, which makes the inter-spin distance sufficient for interaction at room temperature. This is consistent with the decrease in the lattice constant of PFNN10, although the average interatomic distance between B-site ions, i.e., Fe, Ni, and Nb, may be approximately 4 Å when the lattice constant is considered.

Neutron powder diffraction (NPD) patterns were measured along with pair distribution function (PDF) profiles of PFNN10 to determine the superiority of its magnetic properties and its distinctive atomic structure (see Figs. 5 and S5 in the [supplementary material](#)) at room temperature. Structural refinements were performed based on four models: R3 m, R3c, Pm3 m, and P4 mm. Among the four models, the PFNN10 long-range structure derived from the Bragg fit [Fig. 5(a)] agrees best with the R3 m model, with a refined lattice constant and an angle of 4.01(6) Å and 90.03 (7)°. This indicates very little rhombohedral distortion (within the resolution of the data), implying that the sizeable magnetic properties of PFNN10 are not primarily from spin canting. However, this model failed to capture some of the features of the local structure identified from the PDF [Fig. 5(b)]. The single peak at approximately 2.0 Å corresponds to the B–O distance in the perovskite structure and indicates no significant displacement of the B-site ions in their oxygen octahedra; i.e., there seems to be a discrepancy

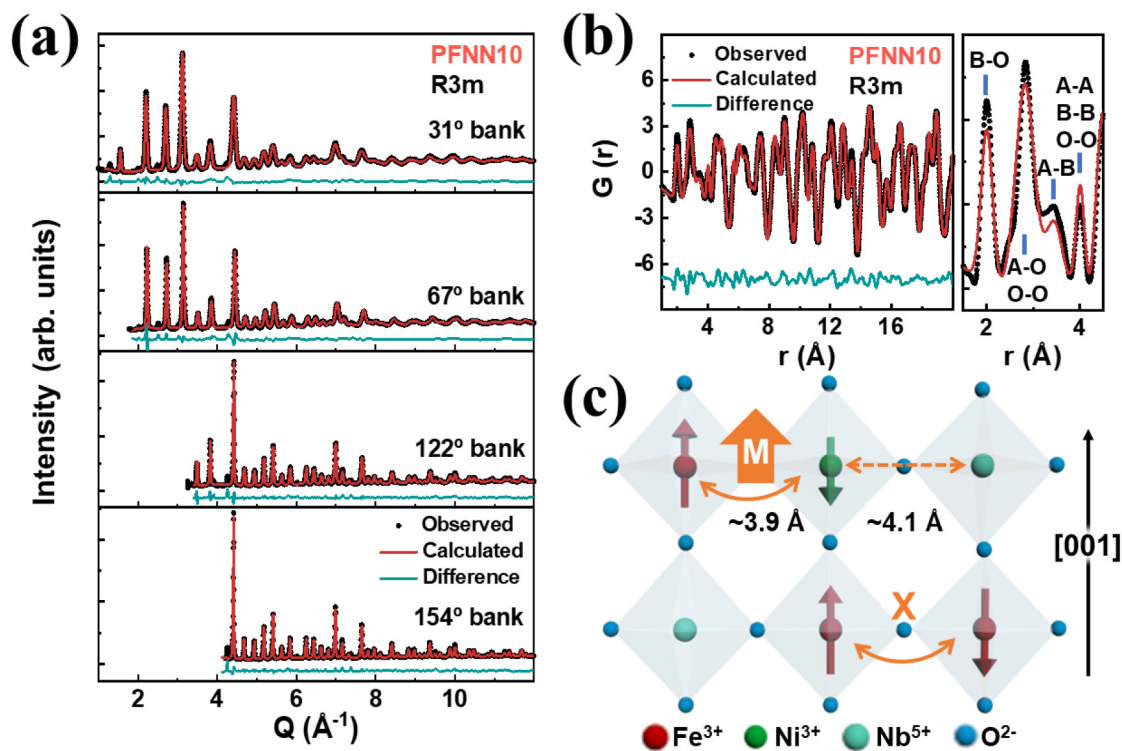


FIG. 5. Room temperature neutron powder diffraction (NPD) of the four highest resolution detector banks of the NOMAD instrument and the neutron pair distribution function (PDF) of PFNN10 at room temperature. (a) Rietveld refinement (for $Q \sim 1\text{--}12\text{ Å}^{-1}$) and (b) small-box modeling (for $r \sim 1\text{--}19\text{ Å}$) profiles were prepared based on the R3m model. The observed and calculated plots together with their difference are shown as a black dot, a red line, and a mint line, respectively. (c) Schematic representation accounting for spin arrangement of PFNN10 by considering the refined NPDF data in combination with the XAS analysis.

between the EXAFS and NPD results. It follows those measurements at lower temperatures, which reduce thermal motion, might be necessary to uncover any static displacements, implying that transition metals can be locally displaced while maintaining an average distance of approximately 4.0 Å.^{55–58} In the long-range structure model derived from the Bragg peaks, other atom–atom neighbors include A–O/O–O distances of approximately 2.8 Å, A–B distances of approximately 3.5 Å, and A–A/B–B/O–O distances of approximately 4.0 Å. In addition to A–O/O–O, there are clear features at approximately 2.50 and 3.20 Å that are most likely the result of the splitting of the A–O peak due to uncorrelated Pb displacements, considering that displacive ferroelectricity in the PFN system is generally caused by Pb displacement along the [111] direction due to the presence of the 6s² lone pair. This is also evidenced by the fact that a large atomic displacement parameter (ADP) was observed for the Pb site in the Bragg fit, suggesting that the A-site of this system is displacive disordered. However, since the crystallographic models tested in this study do not account for A-site displacements, and therefore cannot provide an accurate fit to the local structure, further work needs to be done to develop more complex models to understand these features. Nonetheless, it is possible that the BO₆ octahedra could be locally distorted along the [001] direction and not along the [111] direction, which can be a magnetic easy axis, by considering the split A–O peak together with the reduced rhombohedral distortion and improve electromechanical properties (Fig. 2). This demonstrates that the magnetic spins in PFNN10 could be ferrimagnetically aligned along one direction, i.e., the z-axis, facilitating the survival of magnetic moments arising from the spin cancellation between Fe and Ni ions, as schematically illustrated in Fig. 5(c). While it would be valuable to discuss the precise short-range order of paired Fe and Ni ions, achieving this goal via PDF analysis presented challenges due to the insufficient contrast in the scattering lengths of Fe ($b = 9.45$ fm) and Ni ($b = 10.3$ fm). This limitation made it difficult to accurately determine the chemical ordering. Additionally, obtaining precise chemical ordering of Fe and Ni ions from EXAFS data is challenging due to their random orientation. Nonetheless, despite these challenges in determining the exact short-range ordering, the MH curve and structural data support the mechanism analysis presented in Fig. 5(c).

IV. CONCLUSION

We have demonstrated the significant multiferroic properties of PFNN10, in which the existing Fe ions in the displacive ferroelectric perovskite PFN system were replaced by 10 mol. % Ni ions, resulting from its distinct atomic structure as determined by x-ray and neutron-related analysis. It was found that the magnetic properties peaked along with the magnetoelectric coupling coefficient of the Fe-site-engineered PFN at PFNN10, whereas the ferroelectric properties gradually deteriorated when Ni was introduced due to the phase transition from a non-centrosymmetric to a centrosymmetric system. We discovered that PFNN10 has a unique atomic structure compared to the others. The transition metals located at the B-site are ordered and locally displaced with an interatomic distance of approximately 3.9 Å, which is a relatively smaller value than that of the other compositions that exhibit anti or weak

ferromagnetic properties at room temperature, while maintaining the average distance between the B-site ions of approximately 4.0 Å. It was also found that the oxygen cage could be elongated along the [001] direction, which could act as a magnetic easy axis. Due to their special structure, the magnetic spins with distinct magnetic moments in PFNN10 could be ferrimagnetically arranged along a specific direction, generating a net magnetic moment, resulting in significant magnetic properties even at room temperature. Our discoveries are promising and should be further explored with other multiferroic materials.

SUPPLEMENTARY MATERIAL

See the [supplementary material](#) for additional magnetic/ferroelectric properties, ME coupling, XAS spectra, and NPDP data.

ACKNOWLEDGMENTS

This research was supported by the Material Technology Development Program (No. 1415182019) through the Korea Evaluation Institute of Industrial Technology (KEIT). F.P.M. and M.R.V.J. thank the Danish Agency for Science, Technology, and Innovation for funding the instrument center DanScatt.

AUTHOR DECLARATIONS

Conflict of Interest

The authors have no conflicts to disclose.

Author Contributions

Ji-Hun Park and Jae-Hyeon Cho contributed equally to this work.

Ji-Hun Park: Conceptualization (equal); Data curation (equal); Formal analysis (equal); Investigation (equal); Visualization (equal); Writing – original draft (equal); Writing – review & editing (equal). **Jae-Hyeon Cho:** Conceptualization (equal); Data curation (equal); Formal analysis (equal); Investigation (equal); Methodology (equal); Visualization (equal); Writing – original draft (equal). **Frederick P. Marlton:** Data curation (equal); Investigation (equal); Methodology (equal); Software (equal). **Haeseong Jang:** Data curation (equal); Investigation (equal). **Ju-Hyeon Lee:** Data curation (equal); Methodology (equal). **Jongmoon Jang:** Data curation (equal); Methodology (equal). **Geon-Tae Hwang:** Data curation (equal); Formal analysis (equal). **Abhijit Pramanick:** Data curation (equal); Investigation (equal). **Mads Ry Vogel Jørgensen:** Data curation (equal); Investigation (equal). **Min Gyu Kim:** Data curation (equal); Investigation (equal). **Wook Jo:** Funding acquisition (equal); Project administration (equal); Supervision (equal); Writing – review & editing (equal).

DATA AVAILABILITY

The data that support the findings of this study are available within the article.

23 January 2025 05:53:53

REFERENCES

- ¹N. A. Spaldin and R. Ramesh, *Nat. Mater.* **18**, 203 (2019).
- ²J.-H. Cho and W. Jo, *J. Korean Inst. Electr. Electron. Mater. Eng.* **34**, 149 (2021).
- ³M. Fiebig, T. Lottermoser, D. Meier, and M. Trassin, *Nat. Rev. Mater.* **1**, 16046 (2016).
- ⁴N. A. Spaldin, *Proc. R. Soc. A* **476**, 20190542 (2020).
- ⁵N. Hur, S. Park, P. A. Sharma, J. S. Ahn, S. Guha, and S.-W. Cheong, *Nature* **429**, 392 (2004).
- ⁶T. Choi, S. Lee, Y. J. Choi, V. Kiryukhin, and S. W. Cheong, *Science* **324**, 63 (2009).
- ⁷J. Kreisel and M. Kenzelmann, *Europhys. News* **40**, 17 (2009).
- ⁸J.-M. Hu and C.-W. Nan, *APL Mater.* **7**, 080905 (2019).
- ⁹D. Khomskii, *Physics* **2**, 20 (2009).
- ¹⁰J.-H. Cho, J.-H. Lee, H. Jang, N. J. Lee, W.-S. Kang, G.-T. Hwang, S. Kim, M. G. Kim, and W. Jo, *J. Appl. Phys.* **130**, 094101 (2021).
- ¹¹J. H. Cho, Y. J. Kim, S. H. Kim, Y. J. Lee, J. Y. Choi, G. T. Hwang, J. Ryu, S. K. Kwak, and W. Jo, *J. Am. Ceram. Soc.* **105**, 2655 (2021).
- ¹²J. Wang, J. B. Neaton, H. Zheng, V. Nagarajan, S. B. Ogale, B. Liu, D. Viehland, V. Vaithyanathan, D. G. Schlom, U. V. Waghmare, N. A. Spaldin, K. M. Rabe, M. Wuttig, and R. Ramesh, *Science* **299**, 1719 (2003).
- ¹³T. Kimura, T. Goto, H. Shintani, K. Ishizaka, T. Arima, and Y. Tokura, *Nature* **426**, 55 (2003).
- ¹⁴M. P. Singh, K. D. Truong, S. Jandl, and P. Fournier, *J. Appl. Phys.* **107**, 09D917 (2010).
- ¹⁵J.-H. Park, J.-H. Lee, J.-H. Cho, J. M. Jang, and W. Jo, *J. Korean Inst. Electr. Electron. Mater. Eng.* **35**, 297 (2022).
- ¹⁶N.-R. Ko, J.-H. Cho, J. Jang, and W. Jo, *J. Korean Inst. Electr. Electron. Mater. Eng.* **34**, 386 (2021).
- ¹⁷C. Lu, M. Wu, L. Lin, and J.-M. Liu, *Natl. Sci. Rev.* **6**, 653 (2019).
- ¹⁸S. Dong, H. Xiang, and E. Dagotto, *Natl. Sci. Rev.* **6**, 629 (2019).
- ¹⁹N. A. Hill, *J. Phys. Chem. B* **104**, 6694 (2000).
- ²⁰I. Grinberg and A. M. Rappe, *Phase Transit.* **80**, 351 (2011).
- ²¹I. B. Bersuker and V. Polinger, *Condens. Matter* **5**, 68 (2020).
- ²²S. Picozzi and C. Ederer, *J. Phys.: Condens. Matter* **21**, 303201 (2009).
- ²³M. M. Vopson, *Crit. Rev. Solid State Mater. Sci.* **40**, 223 (2015).
- ²⁴J. B. Goodenough, *J. Solid State Chem.* **127**, 126 (1996).
- ²⁵J. Kanamori, *J. Phys. Chem. Solids* **10**, 87 (1959).
- ²⁶M. Fiebig and N. A. Spaldin, *Eur. Phys. J. B* **71**, 293 (2009).
- ²⁷J. F. Scott, *NPG Asia Mater.* **5**, e72 (2013).
- ²⁸M. G. Kim, H. S. Cho, and C. H. Yo, *J. Phys. Chem. Solids* **59**, 1369 (1998).
- ²⁹J. J. Rehr, A. Ankudinov, and S. I. Zabinsky, *Catal. Today* **39**, 263 (1998).
- ³⁰A. A. Coelho, *J. Appl. Crystallogr.* **51**, 210 (2018).
- ³¹L. F. Henrichs, O. Cespedes, J. Bennett, J. Landers, S. Salamon, C. Heuser, T. Hansen, T. Helbig, O. Gutfleisch, D. C. Lupascu, H. Wende, W. Kleemann, and A. J. Bell, *Adv. Funct. Mater.* **26**, 2111 (2016).
- ³²A. Levstik, V. Bobnar, C. Filipič, J. Holc, M. Kosec, R. Blinc, Z. Trontelj, and Z. Jagličič, *Appl. Phys. Lett.* **91**, 012905 (2007).
- ³³S. Chillal, M. Thede, F. J. Litterst, S. N. Gvasaliya, T. A. Shaplygina, S. G. Lushnikov, and A. Zheludev, *Phys. Rev. B* **87**, 220403 (2013).
- ³⁴S.-W. Cheong, D. Talbayev, V. Kiryukhin, and A. Saxena, *npj Quantum Mater.* **3**, 19 (2018).
- ³⁵M. Mostovoy, *Phys. Rev. Lett.* **96**, 067601 (2006).
- ³⁶Y. Tokura, S. Seki, and N. Nagaosa, *Rep. Prog. Phys.* **77**, 076501 (2014).
- ³⁷Y. Tokura and S. Seki, *Adv. Mater.* **22**, 1554 (2010).
- ³⁸S.-W. Cheong and M. Mostovoy, *Nat. Mater.* **6**, 13 (2007).
- ³⁹T. Moriya, *Phys. Rev.* **120**, 91 (1960).
- ⁴⁰I. Dzyaloshinsky, *J. Phys. Chem. Solids* **4**, 241 (1958).
- ⁴¹I. A. Sergienko and E. Dagotto, *Phys. Rev. B* **73**, 094434 (2006).
- ⁴²R. A. U. Rahman, D. E. Jain Ruth, S. Chakravarty, P. Schmid-Beurmann, D. Duraisamy, G. N. Venkatesan, P. Zhou, G. Srinivasan, and R. Murugan, *J. Appl. Phys.* **126**, 044103 (2019).
- ⁴³T. Nagamiya, K. Yosida, and R. Kubo, *Adv. Phys.* **4**, 1 (1955).
- ⁴⁴C. Zener, *Phys. Rev.* **81**, 440 (1951).
- ⁴⁵J. H. Cho, S. Cho, J. H. Lee, H. Palneedi, J. H. Lee, H. P. Kim, N. J. Lee, S. Tigunta, S. Pojprapai, S. Kim, J. Ryu, Y. S. Oh, S. Hong, and W. Jo, *J. Am. Ceram. Soc.* **104**, 6384 (2021).
- ⁴⁶S. M. M. Zamani and K. Behdinan, *Ceram. Int.* **43**, 12239 (2017).
- ⁴⁷H. Meštrić, R. A. Eichel, T. Kloss, K. P. Dinse, S. Laubach, S. Laubach, P. C. Schmidt, K. A. Schönau, M. Knapp, and H. Ehrenberg, *Phys. Rev. B* **71**, 134109 (2005).
- ⁴⁸J.-H. Cho, J.-H. Lee, J.-H. Park, H. Jang, H.-L. Yu, J. Jang, G.-T. Hwang, M. G. Kim, and W. Jo, *Appl. Phys. Lett.* **122**, 112906 (2023).
- ⁴⁹J. van Bokhoven, *Phys. Chem. Chem. Phys.* **12**, 5502 (2010).
- ⁵⁰P. Li, Y. Wang, and I. W. Chen, *Ferroelectrics* **158**, 229 (2011).
- ⁵¹A. Mesquita, B. M. Fraygola, V. R. Mastelaro, and J. A. Eiras, *Appl. Phys. Lett.* **100**, 172907 (2012).
- ⁵²D. H. Kim, H. J. Lee, G. Kim, Y. S. Koo, J. H. Jung, H. J. Shin, J. Y. Kim, and J. S. Kang, *Phys. Rev. B* **79**, 033402 (2009).
- ⁵³Y.-H. Huang, G. Liang, M. Croft, M. Lehtimäki, M. Karppinen, and J. B. Goodenough, *Chem. Mater.* **21**, 2319 (2009).
- ⁵⁴K. Asokan, Y. S. Chen, C. W. Pao, H. M. Tsai, C. W. O. Lee, C. H. Lin, H. C. Hsueh, D. C. Ling, W. F. Pong, J. W. Chiou, M. H. Tsai, O. Peña, and C. Moure, *Appl. Phys. Lett.* **95**, 131901 (2009).
- ⁵⁵S. A. Ivanov, R. Tellgren, H. Rundlof, N. W. Thomas, and S. Ananta, *J. Phys.: Condens. Matter* **12**, 2393 (2000).
- ⁵⁶A. Palewicz, R. Przenioslo, I. Sosnowska, and A. W. Hewat, *Acta Crystallogr. B* **63**, 537 (2007).
- ⁵⁷F. P. Marlton, Z. Zhang, Y. Zhang, T. E. Proffen, C. D. Ling, and B. J. Kennedy, *Chem. Mater.* **33**, 1407 (2021).
- ⁵⁸M. Winterer, R. Delaplane, and R. McGreevy, *J. Appl. Crystallogr.* **35**, 434 (2002).